Advances in Water Resources 95 (2016) 246–253

Contents lists available at ScienceDirect

Advances in Water Resources

journal homepage: www.elsevier.com/locate/advwatres

3D Mapping of calcite and a demonstration of its relevance to permeability evolution in reactive fractures

Brian R. Ellis [a,*], Catherine A. Peters [b]

[a] Department of Civil and Environmental Engineering, University of Michigan, Ann Arbor, MI, United States
[b] Department of Civil and Environmental Engineering, Princeton University, Princeton, NJ, United States

ARTICLE INFO

Article history:
Available online 6 August 2015

Keywords:
X-ray computed tomography
Calcite dissolution
Fracture permeability
CO_2 sequestration
Reactive transport

ABSTRACT

There is a need to better understand reaction-induced changes in fluid transport in fractured shales, caprocks and reservoirs, especially in the context of emerging energy technologies, including geologic carbon sequestration, unconventional natural gas, and enhanced geothermal systems. We developed a method for 3D calcite mapping in rock specimens. Such information is critical in reactive transport modeling, which relies on information about the locations and accessible surface area of reactive minerals. We focused on calcite because it is a mineral whose dissolution could lead to substantial pathway alteration because of its high solubility, fast reactivity, and abundance in sedimentary rocks. Our approach combines X-ray computed tomography (XCT) and scanning electron microscopy. The method was developed and demonstrated for a fractured limestone core containing about 50% calcite, which was 2.5 cm in diameter and 3.5 cm in length and had been scanned using XCT. The core was subsequently sectioned and energy dispersive X-ray spectroscopy was used to determine elemental signatures for mineral identification and mapping. Back-scattered electron microscopy was used to identify features for co-location. Finally, image analysis resulted in characteristic grayscale intensities of X-ray attenuation that identify calcite. This attenuation mapping ultimately produced a binary segmented 3D image of the spatial distribution of calcite in the entire core. To demonstrate the value of this information, permeability changes were investigated for hypothetical fractures created by eroding calcite from 2D rock surfaces. Fluid flow was simulated using a 2D steady state model. The resulting increases in permeability were profoundly influenced by the degree to which calcite is contiguous along the flow path. If there are bands of less reactive minerals perpendicular to the direction of flow, fracture permeability may be an order of magnitude smaller than when calcite is contiguous. These results emphasize the importance of characterizing spatial distribution of calcite in heterogeneous rocks that also contain a similar abundance of less reactive minerals.

1. Introduction

Flow of acidic fluids through reactive fractures can dissolve minerals and increase fracture aperture, but the specific effect on permeability depends on the spatial pattern of mineral dissolution and the resulting fracture geometry. X-ray computed tomography (XCT) has long been a primary method for non-destructive characterization of rock specimens as it allows for the study of fracture geometry as well as pore structure at resolutions ranging from nm to cm spatial scales [1–8]. Although previous studies have used XCT data to characterize mineral spatial distributions in porous rocks (*e.g.*, [5,9–12]), XCT has not yet been applied to characterize calcite distribution along rock fracture surfaces. Here, we present a method for doing this by coupling XCT imaging with scanning electron microscopy (SEM).

In the simplest application, use of XCT data to identify distinct mineral phases relies on using grayscale intensity in the reconstructed tomographic image to classify voxels. The success in doing this depends on the dissimilarity of minerals' X-ray attenuation coefficients, which manifest as varying grayscale voxel intensities. Many minerals do have contrast in their X-ray attenuation coefficients, but one pair that presents a classification challenge is calcite and dolomite [9]. These minerals often co-occur in carbonate rocks. Contrast enhancement of the XCT data may be required to accentuate the small differences in X-ray attenuation of these two minerals. Use of proxy minerals (effectively internal standards) can also help identify unknown mineral phases by identifying minerals with similar X-ray absorption [12]. Mineral-specific X-ray attenuation can be enhanced through use of dual energy scanning to perform differential absorption imaging, a technique that relies on detecting

* Corresponding author. Tel.: +1 734 763 5470.
E-mail address: brellis@umich.edu (B.R. Ellis).

http://dx.doi.org/10.1016/j.advwatres.2015.07.023
0309-1708/

sharp variations in elemental mass attenuation as a function of X-ray energy. These so called *absorption edges* occur at energies where electrons are removed from specific shells of an element of interest, thereby allowing for identification of specific minerals [9,10].

A common challenge in absorption tomography is that because most X-ray sources produce a polychromatic beam, reconstruction artifacts can be introduced, such as beam hardening [5]. Synchrotron XCT imaging allows for use of a high-energy monochromatic beam and is well suited for performing absorption tomography analyses. Synchrotron imaging also allows for the possibility of combining XCT with other non-destructive detection methods, such as X-ray fluorescence [5] and X-ray microdiffraction [13]. However, synchrotrons are not readily accessible to many researchers, so we must continue to look for opportunities to extract more (or better) data from bench-top XCT scanners.

In addition to providing a means of characterizing mineral distributions, XCT is particularly well suited to distinguish void space from mineral matter and thus is an excellent tool for studying the evolution of geometry and apertures in reactive fractures [2–4,14,15]. Previous studies examining mineral dissolution along fracture pathways have highlighted the importance of calcite as a key reactive mineral whose dissolution can control fracture permeability evolution (see *e.g.*, [16] and references therein). Calcite is highly soluble in acidic conditions and it is kinetically fast reacting [17]. In many sedimentary rocks, it is sufficiently abundant that its dissolution can lead to a large increase in the volume of void space thereby enlarging flow pathways. Advancements in experimental protocols now permit for high-resolution 3D imaging of mineral dissolution within a high-pressure vessel in the context of a flow experiment [18], which allows for an even more complete understanding of how μm-scale mineral heterogeneity controls permeability evolution along a fracture during calcite dissolution. Recent studies have demonstrated non-intuitive hydraulic-chemical-mechanical feedbacks during dissolution along fracture pathways. Examples include dissolution of critical asperities leading to fracture closure [19–21], particle mobilization resulting in fracture clogging [22,23], the occurrence of aperture growth versus closure being dependent on complex confining stress-pH relationships [24], and the development of reaction front instabilities in fractured rocks being a function of both the initial aperture distribution and influent fluid chemistry [18,25].

Understanding the coupled processes that govern reactive flow in fractures has become a high priority with new developments in subsurface resource utilization, including geologic CO_2 sequestration, unconventional natural gas extraction, and geothermal energy production. For the case of geologic CO_2 sequestration, the low permeability caprock formations that overlie the injection reservoir and prevent the upward migration of CO_2 may be susceptible to dissolution by the CO_2-acidified brine. Confirming the long-term storage security of injected CO_2 therefore requires the ability to accurately model CO_2-water-rock interactions, and the resultant evolution of caprock integrity [26–29].

Although the ability to image materials has recently advanced at a fairly rapid pace, computational capabilities (*e.g.*, parallel computing) have advanced even faster. Reactive transport models have been developed that account for reaction-induced changes in fluid transport in fractured and porous media [30–36]. The computational power of these models is driving the need to characterize natural heterogeneities in mineral spatial distributions at the μm to cm scale in order to improve predictive capabilities.

Here, we present a method for coupling XCT imaging with SEM to determine 3D calcite spatial distribution within natural rock samples. This characterization method relies on the ability to determine mineral elemental compositions via energy dispersive X-ray spectroscopy (EDS) of thin sections. Backscattered electron (BSE) imaging is used to co-locate the section in the 3D XCT image. The EDS mineral mapping is then correlated with grayscale pixel intensity of the XCT image to infer 3D mineral spatial distribution in the rock sample. The method was developed, and is demonstrated here, to determine calcite distribution within a carbonate-rich caprock specimen. We focused solely on identifying calcite as it is both ubiquitous in many relevant sedimentary rocks and has been demonstrated to be a key factor in determining fracture permeability evolution during contact with acidic fluids [16].

To demonstrate how this calcite segmentation method would be useful, we applied a 2D steady state flow model to simulate flow in hypothetical fractures undergoing calcite dissolution. Four model scenarios were considered. In three of these, calcite is distributed along the fracture as informed by the XCT-SEM calcite identification analysis described herein. The other scenario assumed that an equivalent amount of calcite is homogeneously distributed along the fracture face. Comparison of the predicted permeability changes helps to understand the influence of accounting for realistic spatial distributions of calcite along a reactive fracture when investigating dissolution-driven changes in fracture geometry.

2. Methods

2.1. Rock specimen, XRD analysis, and XCT scan

The rock core used to develop and demonstrate the combined imaging method is from the Amherstburg limestone in northern Michigan and was collected from a depth of 928 m. The Amherstburg is a low permeability fossiliferous wackestone. This formation serves as the primary caprock for a pilot CO_2 injection project that was conducted as part of the U.S. Department of Energy's Midwest Regional Carbon Sequestration Partnership [37]. Core specimens from this limestone have been previously studied in reactive core flooding experiments with CO_2-acidified brine [4,23], and the fractured cores were subjected to XCT scanning as part of those studies. In this paper, we present a follow-up analysis of one of those experimental cores. The core was scanned on a MicroXCT-400 scanner (Xradia, Inc., Pleasanton, CA) with an X-ray beam energy and power of 150 keV and 10 W, respectively, at rotational increments of 0.14°. The selected optics provided a 3D reconstructed image with a resolution of 27 μm in all dimensions. The 3D XCT dataset (shown in Fig. SI-1) was contrast-adjusted to enhance the grayscale pixel contrast between calcite and dolomite prior to performing the mineral segmentation.

For a small sample from the imaged core, X-ray diffraction (XRD) was used to identify the primary minerals present in the rock and the Rietveld method (JADE) was used to provide semi-quantitative compositional estimates for these minerals. XRD analysis was performed on a Bruker D8 Discover X-Ray Diffractometer. The Amherstburg core was found to contain primarily calcite (51 wt.%) and dolomite group minerals (*i.e.*, $Ca(Mg,Fe,Mn)(CO_3)_2$) (30 wt.%) with minor amounts of quartz (8 wt.%), fluorite (6 wt.%), clay minerals (4 wt.%), and anhydrite (1 wt.%). Since the core examined in this study exhibited visible heterogeneity throughout the 3.5 cm segment (see Fig. 1(a) and (b)), we did not expect to replicate the compositional assemblage estimated by XRD analysis through our combined XCT-SEM analysis. However, this resulting inventory of minerals was used later to guide interpretation of the elemental analyses from X-ray spectroscopy.

2.2. BSE-EDS analysis

Fig. 1 outlines the procedure by which 3D calcite segmentation was achieved through a combined XCT-SEM image analysis method. As shown in Fig. 1(a), after the final 3D XCT scan of the core, it was sectioned and imaged using a scanning electron microscope. All SEM imaging was performed at the Image Analysis Center at Princeton University using a Quanta environmental SEM with an incident beam energy of 15 keV. Using the SEM in backscattered electron mode, a BSE image of size 0.25 mm^2 was generated at a magnification of

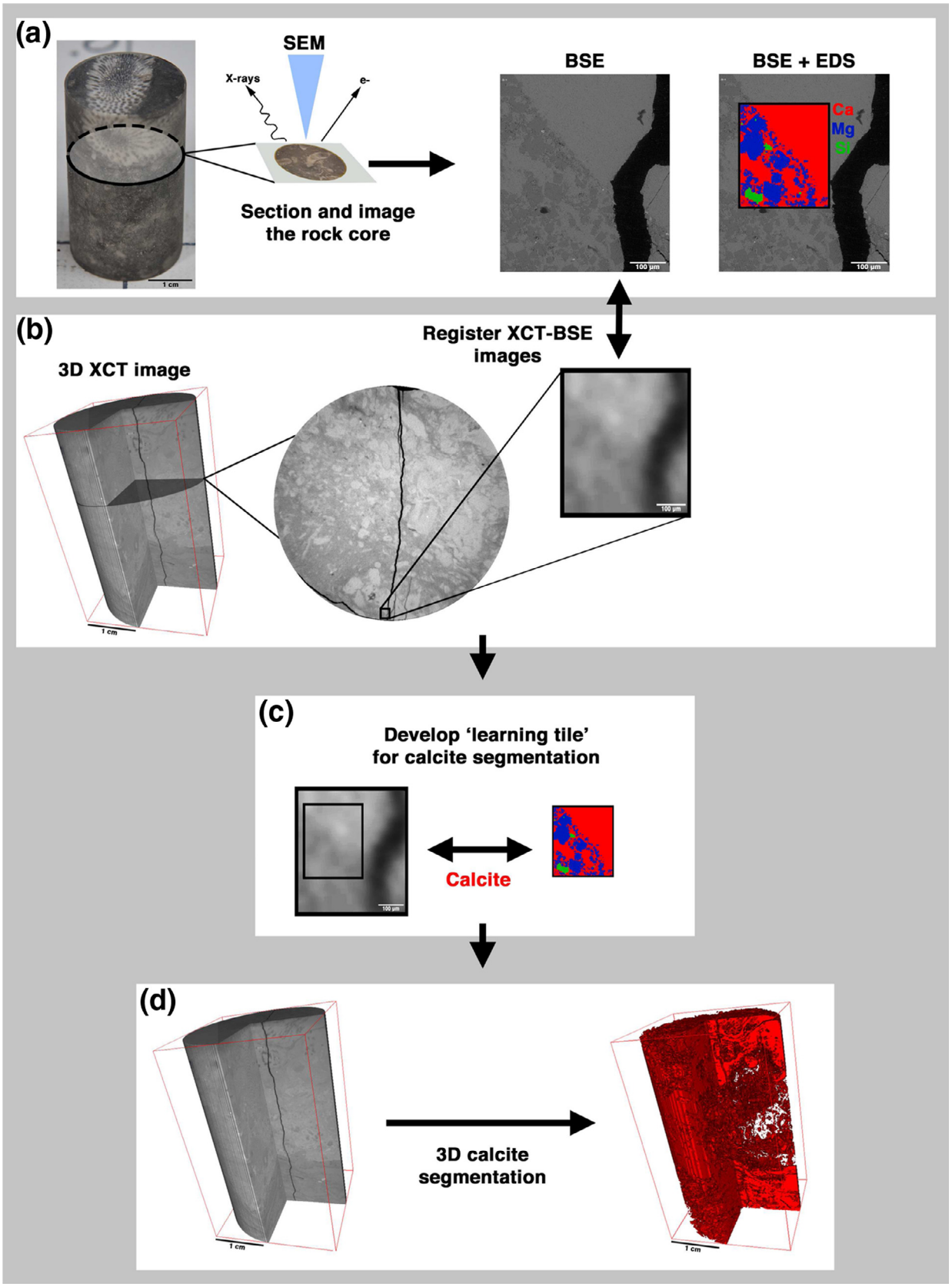

Fig. 1. Depiction of the calcite segmentation method in this study: (a) the original core and the subsequent sectioning and SEM imaging, (b) the 3D XCT image of the core and the co-location of the SEM-imaged section in a 2D XCT slice, (c) development of a 'learning tile' to train the calcite segmentation algorithm, (d) full 3D calcite segmentation of the XCT data set. (For interpretation of the references to color in the text, the reader is referred to the web version of this article.)

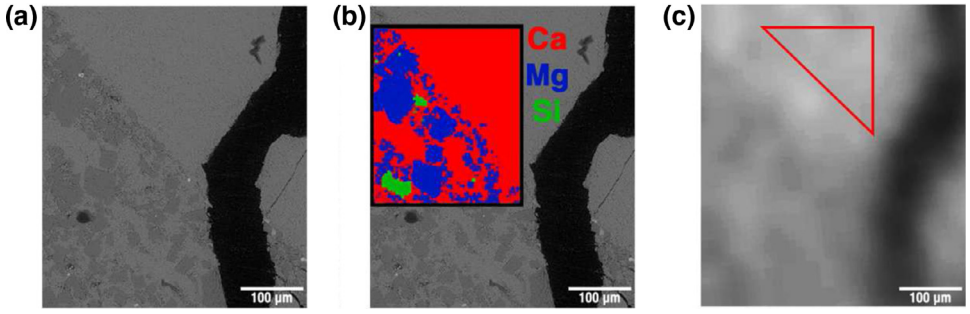

Fig. 2. (a) BSE image of 2D section of the core, (b) EDS elemental maps overlaid on BSE image, (c) calcite voxels identified in XCT data set (interior of red triangle). A larger contiguous calcite pixel region beyond that shown in panel (c) was used to determine a characteristic grayscale range of calcite XCT pixels. (For interpretation of the references to color in this figure legend, the reader is referred to the web version of this article.)

436×, as shown in Fig. 1(a). In this image, we identified distinct features, such as fracture boundaries and unique pore geometries that were later used to register the location with the corresponding 2D XCT image.

EDS, which detects characteristic X-ray emissions from the specimen as a result of the electron beam, was then used to map surface elemental composition of an area roughly the size of 0.1 mm^2 at a resolution of ~3 μm^3, hereafter referred to as the "learning tile". The right hand side of Fig. 1(a) shows the EDS maps for calcium (Ca devoid of Mg, red), magnesium (Mg, blue), and silicon (Si, green) after applying a bicubic smoothing filter to remove noise from the element maps. We used the EDS mapping to identify calcite in the BSE image by locating areas where Ca was the only metal present. The only other elemental signatures present at those locations were carbon and oxygen, thereby confirming that the Ca map corresponded to locations where calcite was present. Ca was also present at all locations where Mg was recorded, suggesting that the Mg EDS map corresponded to the mineral dolomite ($CaMg(CO_3)_2$). Quartz was identified by locating regions where only Si and O were present. Although XRD data shows the presence of (Fe,Mn)-dolomite, anhydrite, fluorite, and clays, these minerals were not observed within the examined learning tile region.

2.3. Calcite identification and image segmentation

Distinct features that were visible in the BSE image were matched with the identical features in 2D slices of the XCT image in order to register the location of the learning tile region (Fig. 1(b)). We chose a section near the edge of the core along the fracture and looked for the sharp mineral boundary observed in the BSE and XCT images shown in Fig. 1(a). Knowledge of the approximate location along the core where the thin section was taken allowed us to more quickly narrow down the location.

Once the learning tile region was found in the XCT image, the EDS mapping was used to identify areas that correspond to calcite (Fig. 1(c)). Because the X-ray attenuation for calcite does not correspond to a single 'characteristic' grayscale value, we analyzed the set of grayscale values for the voxels located within the areas identified as calcite. This process is demonstrated in Fig. 2 with Fig. 2(c) showing a region in the XCT data that corresponds to calcite. We chose this contiguous region (extending beyond the limited selection identified in Fig. 2(c)) of XCT data to determine a distribution of grayscale values corresponding to calcite. The distribution, which is given in the inset of Fig. SI-1 in the supplementary information, was approximately Gaussian, so we chose to use the mean grayscale value from this data plus or minus two standard deviations ($\mu_{cal} \pm 2\sigma$) to determine threshold grayscale intensities for binary classification of voxels as either *calcite* or *not calcite*. This calcite segmentation approach was then applied to the entire set of Amherstburg core XCT data to generate a 3D map of calcite within the core (Fig. 1(d)).

2.4. 2D steady state flow modeling

The model system was a hypothetical fracture in which the adjacent surfaces of the fracture had calcite distributed according to a selected 2D slice from the 3D calcite-segmented image. We investigated three 2D sections (designated as fractures A, B, and C) parallel to the original experimental fracture. The three segmented fracture surfaces differed in the calcite content and the degree to which calcite is contiguous along the direction of flow. For comparison, a fourth scenario was examined using a fracture with spatially uniform calcite distribution (fracture U).

Flow simulations were conducted to investigate permeability evolution for equivalent increases in fracture volume. For all of the fracture scenarios, the base case was flow in a fracture with a uniform aperture of 50 μm. The next two cases corresponded to a doubling ("2×") and ten-fold increase in fracture volume ("10×"). For fracture U, the fracture enlargement was spatially uniform, representing the scenario where calcite is present everywhere at some constant percent. For fractures A, B, and C, the fracture was enlarged only at pixels that contained calcite according to the binary calcite segmentation maps. The spatial resolution for flow modeling was reduced to 108 μm to improve computational efficiency. This grid resolution captures larger mineral grains and contiguous regions of calcite, but is too coarse to differentiate intermixed mineralogy with grain sizes below 27 μm. We did not perform reactive transport modeling in the study, but instead chose this simple approach of eroding calcite with no time dimension. This approach represents reaction progress for a dissolution scenario where a certain volume of calcite is dissolved along a fracture pathway and assumes stable reaction fronts and homogeneous calcite dissolution.

The flow modeling approach used in this study follows the work of James and Chrysikopoulos [38], for 2D single-phase steady state flow in a variable aperture fracture. We have previously used this approach to describe fluid transport in fractures with spatially variable dissolution patterns [8,39]. Flow is induced by setting constant pressure boundary conditions at the inlet and outlet of the fracture so as to create a constant pressure drop across the flow path. No-flow boundary conditions are assigned to the lateral boundaries of the fracture and along the fracture walls, since it is also assumed that there is no flow into or out of the rock matrix. The pressure at each grid cell is calculated by solving the governing flow equation through use of a five-point central finite difference numerical approximation. The velocity within each grid cell is assumed uniform across the aperture dimension.

Fracture permeability, k, is inferred by first relating the volumetric flow rate, Q, for a given differential pressure, ΔP, to an equivalent hydraulic aperture, b_h, according to the cubic law for flow between

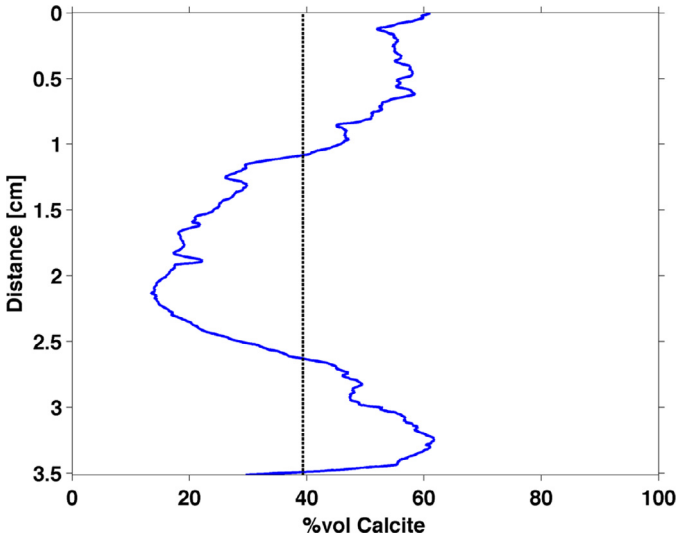

Fig. 3. Transverse averages of calcite content (vol.%) along the length of the core (blue). The dashed line is the average vol.% calcite in the entire core. (For interpretation of the references to color in this figure legend, the reader is referred to the web version of this article.)

two parallel plates [40]

$$b_h = 3\sqrt{\frac{12\mu LQ}{\Delta Pw}} \tag{1}$$

where μ is the viscosity of the fluid, L is the length of the fracture, and w is the fracture width. This hydraulic aperture is then used to estimate fracture permeability by combining the cubic law with Darcy's law

$$k = \frac{b_h^2}{12} \tag{2}$$

3. Results and discussion

3.1. Calcite segmentation

Visual inspection of the XCT image of the Amherstburg core reveals obvious mineral spatial heterogeneity in the rock (Fig. 1(a)). Marine fossils and sediment banding are evident. When the calcite segmentation algorithm was applied to the full 3D XCT data set, a binary 3D image of calcite was generated, as shown in Fig. 1(d). By voxel counts, the overall percentage of calcite within the core was determined to be 39 vol.%. Given that the segmentation method may not capture 100% of the calcite present in the core (see Section 3.3), this estimate of calcite content is reasonable in comparison to the XRD measurement of 51 wt.%, assuming the density of the core is approximately uniform such that vol.% ≅ wt.%. Fig. 3 shows the resulting calcite content along the length of the core. This particular core has a large non-calcite region in the middle of the core. The non-uniform distribution of calcite along the length of the core illustrates the potential importance in being able to capture the spatial variability of reactive minerals along a fracture surface, as flow path alteration may depend heavily on calcite spatial distribution.

The 2D slice of the XCT image for one of the simulated fractures, B, is shown in Fig. 4(d). The calcite-segmented images for all three hypothetical fractures are shown in panels of Fig. 4(a)–(c). The large non-calcite region is evident. By pixel counts, fracture A contains 45% calcite, while fractures B and C contain 46% and 30% calcite, respectively. For fracture B, the transverse averages of calcite along the length of this slice range from 3% to 92%, which is much greater variation than for the 3D image of the core (Fig. 3).

The primary difference between the three 2D calcite-segmented slices is the degree to which calcite is continuously connected along the flow path. Discontinuity in calcite is evident in panels (a)–(c) of Fig. 4 where contiguously connected calcite is identified by uniform coloration. In fracture A, a contiguous region of calcite is present along the entire flow path, whereas fractures B and C exhibit disconnected calcite regions along the length of the fracture. Contiguous calcite regions were identified via a connected component labeling method, *bwlabel*, available in the MATLAB Image Processing Toolbox.

3.2. Permeability evolution in reactive fractures

Fig. 5 presents a visualization of results from the 2D steady state fracture flow modeling. Panel (a) shows the flow field for an initially uniform fracture with a 50 μm fracture aperture, while panels (b) and (c) show the flow fields for eroded fractures (Fracture B) with net fracture volume increases of 2 and 10 times the initial fracture volume, respectively. Initially, flow is uniform along the fracture as would be expected for flow through two parallel smooth plates. Channelling of

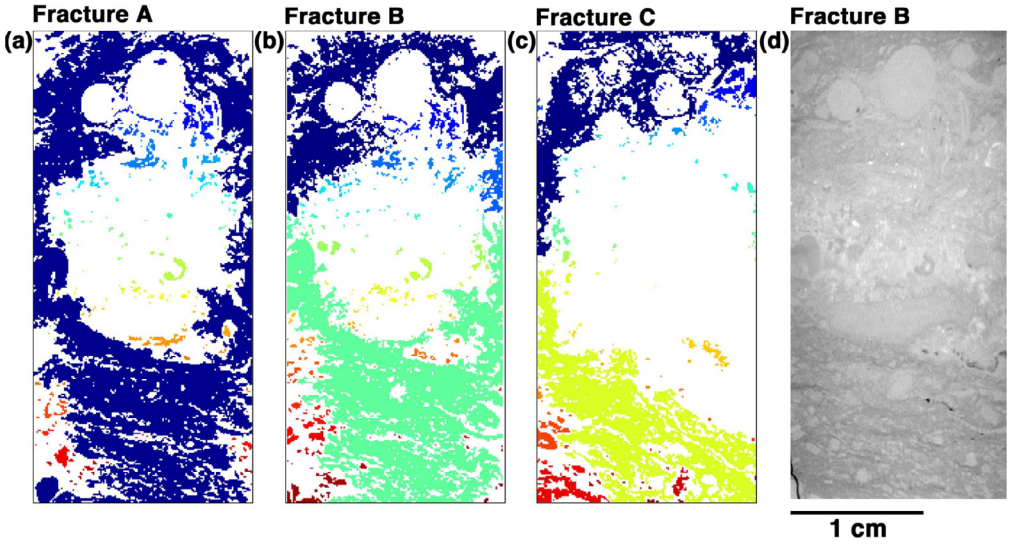

Fig. 4. Color map showing regions of contiguous calcite along 2D fracture pathways for the three theoretical fractures (a)–(c). Each color represents a distinct contiguous calcite region. (d) XCT data 2D section (Fracture B). (For interpretation of the references to color in this figure legend, the reader is referred to the web version of this article.)

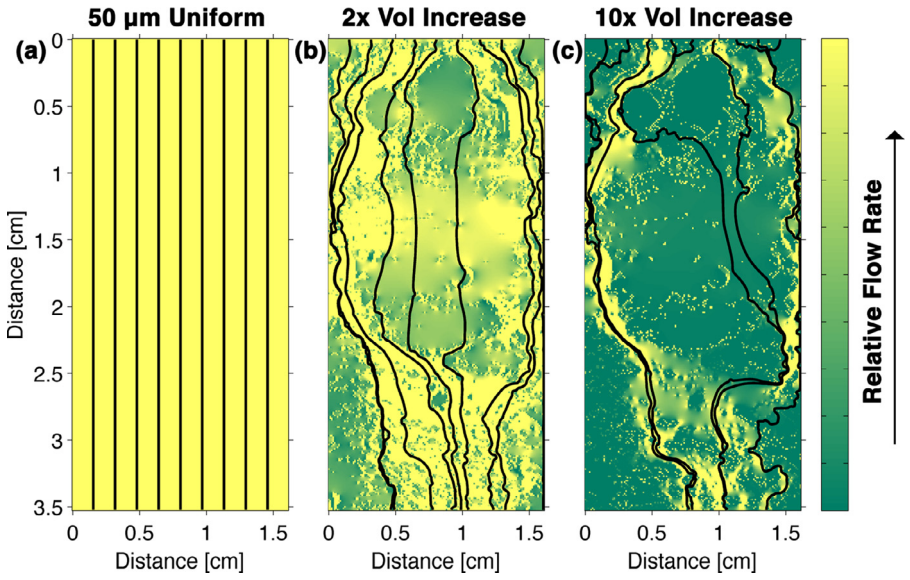

Fig. 5. Simulated flow of water through (a) uniform 50 µm aperture fracture, (b) fracture B with 2× increase in total fracture volume due to calcite erosion (c) fracture B with 10× increase in fracture volume. The colormap depicts gradations in the flowrate relative to the net flow rate through the fracture. Streamlines represent the particle travel paths through the fracture. Particles are released at the top of the each figure, with flow occurring from top to bottom. (For interpretation of the references to color in this figure legend, the reader is referred to the web version of this article.)

flow during calcite-specific dissolution is evidenced by areas of concentration of the flow (lighter color) and the streamlines.

This fluid channelling might erroneously be interpreted as wormhole development as has been observed in carbonate-rich caprocks [41] and in fractured limestones exposed to flow of CO_2-acidified brine [18]. The channels simulated here arise for a different reason. The mineralogically heterogeneous nature of the rock prevents the development of contiguously eroding flow pathways and results in an increase in fracture surface roughness. Zones of constriction remain along the eroding surface and prevent large increases in fracture permeability due to calcite dissolution. These regions represent the presence of less-reactive minerals such as quartz and dolomite. In some instances, they occur perpendicular to the direction of flow. This is evident in Fig. 4, which shows the lack of calcite contiguity along the lengths of two of the three 2D sections examined (fractures B and C).

Fig. 6 presents permeability estimates for the simulated fractures. Fracture permeability is predicted to increase by two orders of magnitude for a 10× increase in fracture volume when it is assumed that

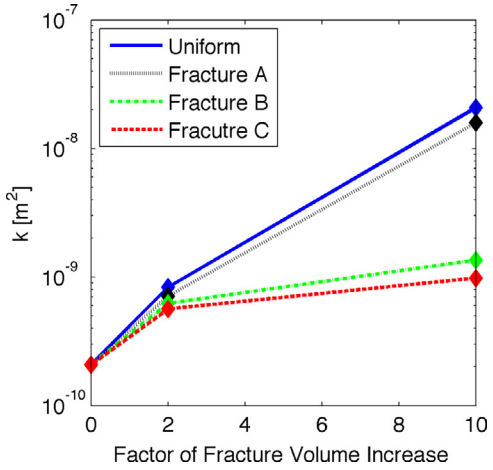

Fig. 6. Estimated permeability as a function of equivalent increases in fracture volume for the modeled calcite dissolution scenarios (diamonds).

dissolution occurs uniformly along the entire fracture. When the true spatial distribution of calcite is accounted for, lower increases in fracture permeability are predicted for all three simulated fractures. Spatially non-uniform dissolution along fracture A, which has a higher degree of calcite contiguity along the flow path, resulted in a final fracture permeability on the same order of magnitude as the uniform dissolution scenario (fracture U). Whereas for fractures B and C, where calcite is not contiguous, an equivalent 10× increase in total fracture volume led to an increase in permeability by only a factor of 6.5 and 4.7, respectively. This result emphasizes the potential influence of crosscutting bands or regions of less reactive minerals in controlling fracture permeability during reactive flows. The spatially non-uniform dissolution will also result in more tortuous flow through the fracture and increased surface roughness, both of which will impede flow through the dissolving fracture.

For the particular core examined in this study, neglecting to account for the actual distribution of calcite along a fracture surface could potentially lead to an overestimation of fracture permeability by more than an order of magnitude due to such occurrences of less reactive minerals perpendicular to the direction of flow. If the rock in question had a more spatially homogeneous mineralogical composition, such as that of an oolitic limestone, then we might expect reaction front instabilities to develop and wormhole generation to take place [42,43]. This could result in permeability increases larger than those predicted for the spatially uniform dissolution scenario [44].

3.3. Additional considerations

The calcite segmentation algorithm developed here may identify regions as being *not calcite* when in fact they may contain some amount of calcite, but at a spatial scale smaller than our XCT resolution. In a previous study it was observed that when calcite is tightly mixed with other minerals such as dolomite, fracture aperture growth is limited because the slow dissolution of the less reactive mineral phases controls aperture size [4]. When calcite is mixed with other slower reacting minerals (*e.g.*, dolomite, quartz, clays), calcite-depleted microporous zones can develop [3,4,36]. These matrices can preserve the original aperture even after extensive calcite dissolution [39]. Thus, if the goal is to predict flow path alterations, it is not

necessarily a problem that this mineral characterization method does not identify the calcite that is intricately mixed with other less reactive minerals.

For other purposes of 3D mineral mapping, such as to predict fracture rheology (*e.g.*, [45,46]), sub-voxel characterizations could be important. One might employ the same image segmentation approach used here but recognize that when features of interest are at sub-voxel resolution the grayscale voxel intensity will represent an average of multiple different features. The combined XCT-SEM approach used in this study may be able to capture these partial volume effects by utilizing mixed phase regions at coarser voxel resolutions to train the segmentation algorithm. Alternatively, finer XCT and element mapping resolutions may allow for better characterization of less abundant phases (*e.g.*, clays) or identification of solid-solution phases (*e.g.*, $Ca(Mg,Fe)(CO_3)_2$) where substituted elements may be difficult to detect.

Future application of the 3D mineral segmentation method presented here could be optimized to provide higher confidence in the range of grayscale pixel intensities used to segment calcite from the rest of the minerals within a particular sample. To do this, we suggest sectioning the original core at several different locations and examining multiple sites within each. This would allow one to generate a larger number of learning tiles that would then be used to establish the grayscale intensity range used to identify calcite voxels within the 3D XCT data set. Doing this may alleviate XCT imaging artifacts and improve confidence in the segmentation-training step prior to using the segmented data in reactive transport model simulations. One might also consider how mineral spatial distributions change as a function of depth from the surface of a fracture, as here we used a simplifying assumption that 2D mineral distributions were unchanged as dissolution progressed. Adding this layer of complexity would also require that fracture flow be modeled in 3D.

4. Conclusion

Here we demonstrated a method for combining two complementary imaging techniques in order to infer the 3D distribution of calcite in experimental cores with XCT data sets. This technique relies on the ability to identify calcite in 2D SEM images and register these images to corresponding locations within the 3D XCT data, to train a mineral segmentation algorithm that can be applied to the entire XCT data set. The rationale for focusing on calcite is that it plays a significant role in determining the evolution of fracture geometry and permeability, and is relevant in many reactive fracture scenarios in the subsurface. Application of the calcite segmentation approach to a core specimen of a limestone caprock revealed significant spatial variability in calcite content.

In applying the resulting calcite maps to fracture geometry evolution scenarios, we demonstrated that when calcite distribution along a fracture pathway is not taken into account, dissolution-driven permeability increases might be overestimated. The flow modeling demonstrates the utility of applying this 3D mineral characterization method when trying to predict reaction-induced permeability evolution in a fracture.

Even though reactive transport simulations were not carried out here, that is the type of application where fracture surface mineral mapping would be very useful. The case of CO_2 sequestration is one relevant potential application. If calcite distribution along a caprock fracture is not accurately captured, changes to fracture permeability during a potential CO_2 leakage event may be overestimated. The existence and persistence of bands of less reactive minerals perpendicular to the direction of flow may serve as bottlenecks and constrict flow even during extensive calcite dissolution along a fracture pathway [39]. This fact, coupled with the increase in μm to cm scale fracture surface roughness due to non-uniform dissolution patterns, may restrict the flow of fluids along reactive fractures such that traditional relationships between porosity and permeability may not hold when estimating fracture permeability evolution during periods of dissolution [36].

As bench-scale XCT scanners become ever more commonplace and affordable, many researchers will be able to utilize XCT in efforts to characterize geo-, bio-, and synthetic materials. Synchrotron-based XCT analysis will continue to have advantages over most bench-scale scanners, but the proliferation of bench-scale scanners will allow for easier access to this characterization technique for a large number of researchers. Coupling bench-scale XCT data sets with electron microscopy can serve to augment and improve 3D characterization capabilities. Applications of the 3D mineral segmentation method described in this study may help future researchers examine the influence of mineral spatial heterogeneity on reactive transport in fractured rocks, which has implications for a variety of research fields including many related to emerging subsurface energy activities.

Acknowledgments

This material is based upon work supported by the National Science Foundation under Grant CBET-1214416 to the University of Michigan and by the Department of Energy under Grant DE-FE0023354 to Princeton University (via Penn State University). B.R.E. also acknowledges funding support from the Michigan Society of Fellows. We further acknowledge the use of PRISM Imaging and Analysis Center, which is supported in part by the NSF MRSEC program through the Princeton Center for Complex Materials (Grant DMR-0819860).

Supplementary materials

Supplementary material associated with this article can be found, in the online version, at doi:10.1016/j.advwatres.2015.07.023.

References

[1] Ketcham RA, Carlson WD. Acquisition, optimization and interpretation of X-ray computed tomographic imagery: applications to the geosciences. Comput Geosci 2001;27:381–400. http://dx.doi.org/10.1016/S0098-3004(00)00116-3.
[2] Gouze P, Noiriel C, Bruderer C, Loggia D, Leprovost R. X-ray tomography characterization of fracture surfaces during dissolution. Geophys Res Lett 2003;30:1267. http://dx.doi.org/10.1029/2002GL016755.
[3] Noiriel C, Madé B, Gouze P. Impact of coating development on the hydraulic and transport properties in argillaceous limestone fracture. Water Resour Res 2007;43:W09406. http://dx.doi.org/10.1029/2006WR005379.
[4] Ellis BR, Peters CA, Fitts JP, Bromhal G, McIntyre D, Warzinski R, et al. Deterioration of a fractured carbonate caprock exposed to CO2-acidified brine flow. Greenhouse Gases Sci Technol 2011;1:248–60. http://dx.doi.org/10.1002/ghg.25.
[5] Baker DR, Mancini L, Polacci M, Higgins MD, Gualda GAR, Hill RJ, et al. An introduction to the application of X-ray microtomography to the three-dimensional study of igneous rocks. Lithos 2012;148:262–76. http://dx.doi.org/10.1016/j.lithos.2012.06.008.
[6] Werth CJ, Zhang C, Brusseau ML, Oostrom M, Baumann T. A review of non-invasive imaging methods and applications in contaminant hydrogeology research. J Contam Hydrol 2010;113:1–24. http://dx.doi.org/10.1016/j.jconhyd.2010.01.001.
[7] Wildenschild D, Sheppard AP. X-ray imaging and analysis techniques for quantifying pore-scale structure and processes in subsurface porous medium systems. Adv Water Resour 2013;51:217–46. http://dx.doi.org/10.1016/j.advwatres.2012.07.018.
[8] Technique of Iterative Local Thresholding (TILT) at Princeton University 2015, http://TILT.princeton.edu.
[9] Remeysen K, Swennen R. Application of microfocus computed tomography in carbonate reservoir characterization: possibilities and limitations. Mar Pet Geol 2008;25:486–99. http://dx.doi.org/10.1016/j.marpetgeo.2007.07.008.
[10] Gualda GAR, Pamukcu AS, Claiborne LL, Rivers ML. Quantitative 3D petrography using X-ray tomography 3: documenting accessory phases with differential absorption tomography. Geosphere 2010;6:782–92. http://dx.doi.org/10.1130/GES00568.1.
[11] Golab A, Romeyn R, Averdunk H, Knackstedt M, Senden TJ. 3D characterisation of potential CO2 reservoir and seal rocks. Aust J Earth Sci 2013;60:111–23. http://dx.doi.org/10.1080/08120099.2012.675889.
[12] Ketcham RA, Koeberl C. New textural evidence on the origin of carbonado diamond: an example of 3-D petrography using X-ray computed tomography. Geosphere 2013;9:1336–47. http://dx.doi.org/10.1130/GES00908.1.

[13] Gräfe M, Klauber C, Gan B, Tappero RV. Synchrotron X-ray microdiffraction (μXRD) in minerals and environmental research. Powder Diffr 2014;29:S64–72. http://dx.doi.org/10.1017/S0885715614001031.
[14] Noiriel C, Gouze P, Madé B. 3D analysis of geometry and flow changes in a limestone fracture during dissolution. J Hydrol 2013;486:211–23. http://dx.doi.org/10.1016/j.jhydrol.2013.01.035.
[15] Fitts JP, Ellis BR, Deng H, Peters CA. Geochemical controls on fracture evolution in carbon sequestration. In: 46th US Rock Mechanics/Geomechanics Symposium, 24-27 June 2012. Chicago, IL, USA: American Rock Mechanics Association; 2012, ARMA 12-549.
[16] Fitts JP, Peters CA. Caprock fracture dissolution and CO2 leakage. Rev Mineral Geochem 2013;77:459–79. http://dx.doi.org/10.2138/rmg.2013.77.13.
[17] Chou L, Garrels RM, Wollast R. Comparative study of the kinetics and mechanisms of dissolution of carbonate minerals. Chem Geol 1989;78:269–82. http://dx.doi.org/10.1016/0009-2541(89)90063-6.
[18] Deng H, Fitts JP, Crandall D, McIntyre D, Peters CA. Alterations of fractures in carbonate rocks by CO2-acidified brines. Environ Sci Technol 2015 in press, http://dx.doi.org/10.1021/acs.est.5b01980.
[19] Durham WB, Bourcier WL, Burton EA. Direct observation of reactive flow in a single fracture. Water Resour Res 2001;37:1–12. http://dx.doi.org/10.1029/2000WR900228.
[20] Polak A, Elsworth D, Yasuhara H, Grader AS, Halleck PM. Permeability reduction of a natural fracture under net dissolution by hydrothermal fluids. Geophys Res Lett 2003;30:2020. http://dx.doi.org/10.1029/2003GL017575.
[21] Ameli P, Elkhoury JE, Morris JP, Detwiler RL. Fracture permeability alteration due to chemical and mechanical processes: a coupled high-resolution model. Rock Mech Rock Eng 2014;47:1563–73. http://dx.doi.org/10.1007/s00603-014-0575-z.
[22] Newell DL, Carey JW. Experimental evaluation of wellbore integrity along the cement-rock boundary. Environ Sci Technol 2013;47:276–82. http://dx.doi.org/10.1021/es3011404.
[23] Ellis BR, Fitts J, Bromhal G, McIntyre D, Tappero R, Peters CA. Dissolution-driven permeability reduction of a fractured carbonate caprock. Environ Eng Sci 2013;30:187–93. http://dx.doi.org/10.1089/ees.2012.0337.
[24] Ishibashi T, McGuire TP, Watanabe N, Tsuchiya N, Elsworth D. Permeability evolution in carbonate fractures: competing roles of confining stress and fluid pH. Water Resour Res 2013;49:2828–42. http://dx.doi.org/10.1002/wrcr.20253.
[25] Szymczak P, Ladd AJC. The initial stages of cave formation: beyond the one-dimensional paradigm. Earth Planet Sci Lett 2011;301:424–32. http://dx.doi.org/10.1016/j.epsl.2010.10.026.
[26] Shukla R, Ranjith P, Haque A, Choi X. A review of studies on CO2 sequestration and caprock integrity. Fuel 2010;89:2651–64. http://dx.doi.org/10.1016/j.fuel.2010.05.012.
[27] Bildstein O, Kervévan C, Lagneau V, Delaplace P, Crédoz A, Audigane P, et al. Integrative modeling of caprock integrity in the context of CO_2 storage: evolution of transport and geochemical properties and impact on performance and safety assessment. Oil Gas Sci Technol – Rev L'Institut Fr Pétrole 2010;65:485–502. http://dx.doi.org/10.2516/ogst/2010006.
[28] Elkhoury JE, Detwiler RL, Ameli P. Can a fractured caprock self-heal? Earth Planet Sci Lett 2015;417:99–106. http://dx.doi.org/10.1016/j.epsl.2015.02.010.
[29] Bielicki JM, Peters CA, Fitts JP, Wilson EJ. An examination of geologic carbon sequestration policies in the context of leakage potential. Int J Greenhouse Gas Control 2015;37:61–75. http://dx.doi.org/10.1016/j.ijggc.2015.02.023.
[30] MacQuarrie KTB, Mayer KU. Reactive transport modeling in fractured rock: a state-of-the-science review. Earth-Sci Rev 2005;72:189–227. http://dx.doi.org/10.1016/j.earscirev.2005.07.003.
[31] Li L, Steefel CI, Yang L. Scale dependence of mineral dissolution rates within single pores and fractures. Geochim Cosmochim Acta 2008;72:360–77. http://dx.doi.org/10.1016/j.gca.2007.10.027.
[32] Kang Q, Lichtner PC, Viswanathan HS, Abdel-Fattah AI. Pore scale modeling of reactive transport involved in geologic CO2 sequestration. Transp Porous Media 2010;82:197–213. http://dx.doi.org/10.1007/s11242-009-9443-9.
[33] Nogues JP, Fitts JP, Celia MA, Peters CA. Permeability evolution due to dissolution and precipitation of carbonates using reactive transport modeling in pore networks. Water Resour Res 2013;49:6006–21. http://dx.doi.org/10.1002/wrcr.20486.
[34] Molins S, Trebotich D, Yang L, Ajo-Franklin JB, Ligocki TJ, Shen C, et al. Pore-scale controls on calcite dissolution rates from flow-through laboratory and numerical experiments. Environ Sci Technol 2014;48:7453–60. http://dx.doi.org/10.1021/es5013438.
[35] Pandey SN, Chaudhuri A, Kelkar S, Sandeep VR, Rajaram H. Investigation of permeability alteration of fractured limestone reservoir due to geothermal heat extraction using three-dimensional thermo-hydro-chemical (THC) model. Geothermics 2014;51:46–62. http://dx.doi.org/10.1016/j.geothermics.2013.11.004.
[36] Chen L, Kang Q, Viswanathan HS, Tao W-Q. Pore-scale study of dissolution-induced changes in hydrologic properties of rocks with binary minerals. Water Resour Res 2014;50:9343–65. http://dx.doi.org/10.1002/2014WR015646.
[37] Sminchak J, Gupta N, Gerst J. Well test results and reservoir performance for a carbon dioxide injection test in the Bass Islands Dolomite in the Michigan Basin. Environ Geosci 2009;16:153–62. http://dx.doi.org/10.1306/eg.04080909001.
[38] James SC, Chrysikopoulos CV. Transport of polydisperse colloids in a saturated fracture with spatially variable aperture. Water Resour Res 2000;36:1457–65. http://dx.doi.org/10.1029/2000WR900048.
[39] Deng H, Ellis BR, Peters CA, Fitts JP, Crandall D, Bromhal GS. Modifications of carbonate fracture hydrodynamic properties by CO2-acidified brine flow. Energy Fuels 2013;27:4221–31. http://dx.doi.org/10.1021/ef302041s.
[40] Zimmerman RW, Bodvarsson GS. Hydraulic conductivity of rock fractures. Transp Porous Media 1996;23:1–30. http://dx.doi.org/10.1007/BF00145263.
[41] Smith MM, Sholokhova Y, Hao Y, Carroll SA. Evaporite caprock integrity: an experimental study of reactive mineralogy and pore-scale heterogeneity during brine-CO2 exposure. Environ Sci Technol 2013;47:262–8. http://dx.doi.org/10.1021/es3012723.
[42] Hoefner ML, Fogler HS. Pore evolution and channel formation during flow and reaction in porous media. AIChE J 1988;34:45–54. http://dx.doi.org/10.1002/aic.690340107.
[43] Elkhoury JE, Ameli P, Detwiler RL. Dissolution and deformation in fractured carbonates caused by flow of CO2-rich brine under reservoir conditions. Int J Greenhouse Gas Control 2013;16(Supplement 1):S203–15. http://dx.doi.org/10.1016/j.ijggc.2013.02.023.
[44] Szymczak P, Ladd AJC. Reactive-infiltration instabilities in rocks. Part 2. Dissolution of a porous matrix. J Fluid Mech 2014;738:591–630. http://dx.doi.org/10.1017/jfm.2013.586.
[45] Ikari MJ, Niemeijer AR, Marone C. The role of fault zone fabric and lithification state on frictional strength, constitutive behavior, and deformation microstructure. J Geophys Res Solid Earth 2011;116:B08404. http://dx.doi.org/10.1029/2011JB008264.
[46] Petrovitch CL, Pyrak-Nolte LJ, Nolte DD. Combined scaling of fluid flow and seismic stiffness in single fractures. Rock Mech Rock Eng 2014;47:1613–23. http://dx.doi.org/10.1007/s00603-014-0591-z.